THE ASTROPHYSICAL JOURNAL, 216:947–962, 1977 September 15

A FAST INVARIANT IMBEDDING METHOD FOR MULTIPLE SCATTERING CALCULATIONS AND AN APPLICATION TO EQUIVALENT WIDTHS OF CO_2 LINES ON VENUS

MAKIKO SATO, KIYOSHI KAWABATA, AND JAMES E. HANSEN
NASA Institute for Space Studies, Goddard Space Flight Center
Received 1977 February 7

ABSTRACT

A fast method is developed for numerical solution of the invariant imbedding equation for the reflection function of a plane-parallel layer. The two key ingredients in obtaining the fast solution are application of a τ-integration technique designed for stiff differential equations and explicit use of the fact that the high-frequency Fourier terms arise from the outer skin of the atmosphere. For a homogeneous atmosphere the resulting computing time is approximately a factor of 2 longer than for the efficient "doubling" method; however, for an inhomogeneous atmosphere the method described in this paper is much faster than the "adding" method.

As a sample application we compute the equivalent width of CO_2 absorption lines as a function of phase angle for several models of the atmosphere of Venus. The results indicate that it is essential to incorporate the vertical distributions of pressure and temperature, and thus employ an inhomogeneous model, for a quantitative analysis of atmospheric structure based on absorption-line observations. They also indicate that extraction of the potential detailed information on vertical atmospheric structure contained in spectroscopic measurements will depend on analysis of line shapes and the relative depths of different lines, requiring high spatial resolution. Observations of the equivalent widths of the $R(0)$ lines of the 0.782 μm and 1.049 μm CO_2 bands are consistent with an inhomogeneous atmospheric model in which the cloud particle number density peaks at ~ 55 km, but not with simple homogeneous or reflecting layer models.

Subject headings: planets: atmospheres — planets: Venus — radiative transfer

I. INTRODUCTION

A variety of methods have been developed for computing the intensity of radiation reflected by a planetary atmosphere, or other medium, for a specified source of incident radiation (cf. the review by Hansen and Travis 1974*a*). One of these approaches, the invariant imbedding method, is based on an equation which describes the change in the reflected radiation when an optically thin layer is added to the top of the atmosphere. This equation is used to treat the problem of reflection from a planetary atmosphere as an initial value problem, and in effect build an atmosphere from the ground up.

Ambartsumian (1942) initially derived the invariant imbedding equation for the reflection function. However, he eliminated the derivative of the reflection function by combining that equation with an analogous equation obtained by adding a thin layer to the bottom of the atmosphere; the resulting integral equation is the basis for the method of X and Y functions for a finite atmosphere or the method of H functions for an infinite atmosphere (Ambartsumian 1958; Chandrasekhar 1960). The direct numerical attack on the differential equation, which we refer to as the invariant imbedding method, was developed most extensively by Bellman, Kagiwada, Kalaba, Ueno, Wing, and associates (cf. Hansen and Travis 1974*a* for a list of references).

Although the invariant imbedding method is extremely simple, it has not been used for practical applications to planetary atmospheres as extensively as other methods such as the doubling method. The primary reason is that the computing time is extremely long for the numerical methods of solution that have been published. However, Hansen and Travis (1974*a*) have pointed out that the method could be made more efficient, in which case it would become quite useful for an inhomogeneous atmosphere.

In this paper we describe a fast method for solution of the invariant imbedding equation, make explicit timing comparisons with the doubling method, and make illustrative calculations for inhomogeneous model atmospheres of Venus.

II. INVARIANT IMBEDDING EQUATION

Let $I_\tau(\mu, \phi)$ be the intensity (radiance) diffusely reflected by a plane-parallel layer into the zenith angle $\theta = \cos^{-1}\mu$ and azimuth angle ϕ (cf. Fig. 1). For an arbitrary external illumination $I_0(\mu, \phi)$, I_τ can be expressed in terms of a

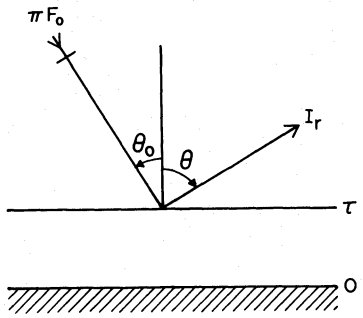

FIG. 1.—Definition of zenith angles and optical depth

reflection function R (which is a matrix if polarization is included):

$$I_r(\mu, \phi) = \frac{1}{\pi}\int_0^1 \mu' d\mu' \int_0^{2\pi} R(\mu, \mu', \phi - \phi') I_0(\mu', \phi') d\phi' \,. \tag{1}$$

If the incident radiation can be approximated as being monodirectional, i.e.,

$$I_0(\mu, \phi) = \delta(\mu - \mu_0)\delta(\phi - \phi_0)\pi F_0 \,, \tag{2}$$

where δ is the Dirac delta function and πF_0 is the incident flux (irradiance) per unit area perpendicular to the incident beam, say in ergs s^{-1} cm^{-2}, then

$$I_r(\mu, \phi) = \mu_0 R(\mu, \mu_0, \phi - \phi_0) F_0 \,. \tag{3}$$

Based on the definition of R given by equation (1), the invariant imbedding equation can be derived by inspection. Suppose a thin layer of optical thickness $\Delta\tau \ll 1$ is added to the top of a layer (which may be inhomogeneous) of optical thickness τ (cf. Fig. 2). Then the reflection function for the total layer, of optical thickness $\tau + \Delta\tau$, is

$$\begin{aligned} R(\tau + \Delta\tau; \mu, \mu_0, \phi - \phi_0) = {} & \left[1 - \frac{\Delta\tau}{\mu}\right] R(\tau; \mu, \mu_0, \phi - \phi_0) \left[1 - \frac{\Delta\tau}{\mu_0}\right] + \frac{\varpi \Delta\tau}{4\mu\mu_0} P(-\mu, \mu_0, \phi - \phi_0) \\ & + \frac{1}{\pi}\int_0^1 \int_0^{2\pi} \mu' R(\tau; \mu, \mu', \phi - \phi') \frac{\varpi \Delta\tau}{4\mu'\mu_0} P(\mu', \mu_0, \phi' - \phi_0) d\mu' d\phi' \\ & + \frac{1}{\pi}\int_0^1 \int_0^{2\pi} \mu' \frac{\varpi \Delta\tau}{4\mu'\mu} P(-\mu, -\mu', \phi - \phi') R(\tau; \mu', \mu_0, \phi' - \phi_0) d\mu' d\phi' \\ & + \frac{1}{\pi}\int_0^1 \int_0^{2\pi} \mu' R(\tau; \mu, \mu', \phi - \phi') \\ & \times \left[\frac{1}{\pi}\int_0^1 \int_0^{2\pi} \mu'' \frac{\varpi \Delta\tau}{4\mu'\mu''} P(\mu', -\mu'', \phi' - \phi'') R(\tau; \mu'', \mu_0, \phi'' - \phi_0) d\mu'' d\phi''\right] d\mu' d\phi' \end{aligned} \tag{4}$$

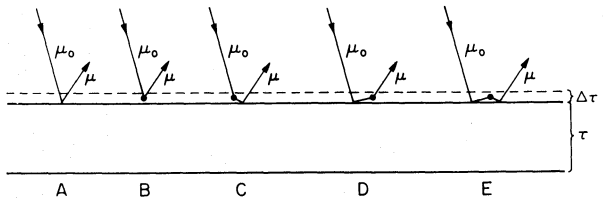

FIG. 2.—Schematic representation of reflection by a plane-parallel layer when a very thin layer ($\Delta\tau \ll 1$) is added to the top of the main layer. There is at most one scattering in the thin layer. The order of the illustrations corresponds to the order of the five terms on the right-hand side of eqs. (4) and (5).

or

$$\frac{\partial R(\tau;\mu,\mu_0,\phi-\phi_0)}{\partial\tau} = -\left(\frac{1}{\mu}+\frac{1}{\mu_0}\right)R(\tau;\mu,\mu_0,\phi-\phi_0) + \frac{\varpi}{4\mu\mu_0}P(-\mu,\mu_0,\phi-\phi_0)$$
$$+\frac{\varpi}{4\pi\mu_0}\int_0^1\int_0^{2\pi}R(\tau;\mu,\mu',\phi-\phi')P(\mu',\mu_0,\phi'-\phi_0)d\mu'd\phi'$$
$$+\frac{\varpi}{4\pi\mu}\int_0^1\int_0^{2\pi}P(-\mu,-\mu',\phi-\phi')R(\tau;\mu',\mu_0,\phi'-\phi_0)d\mu'd\phi'$$
$$+\frac{\varpi}{4\pi}\int_0^1\int_0^{2\pi}R(\tau;\mu,\mu',\phi-\phi')$$
$$\times\left[\frac{1}{\pi}\int_0^1\int_0^{2\pi}P(\mu',-\mu'',\phi'-\phi'')R(\tau;\mu'',\mu_0,\phi''-\phi_0)d\mu''d\phi''\right]d\mu'd\phi', \quad (5)$$

where ϖ is the single scattering albedo in the thin added layer and $P(\mu,\mu_0,\phi-\phi_0)$ is the phase function (or phase matrix, if polarization is included) in that layer.

In the invariant imbedding method, equation (5) is used for numerical computations to build an atmosphere from the ground up. The initial condition is

$$R(0;\mu,\mu_0,\phi-\phi_0) = R_g(\mu,\mu_0,\phi-\phi_0), \quad (6)$$

where R_g is the ground reflectivity, ranging from $R_g = 0$ for a completely absorbing ground to $R_g = 1$ for a conservatively reflecting Lambert surface.

The azimuthal dependence can be handled most efficiently by Fourier expansions of R and P. For simplicity in the following equations let us neglect polarization and assume that P is an even function of $\phi-\phi_0$. The Fourier expansions then have the form

$$R(\tau,\mu,\mu_0,\phi-\phi_0) = \sum_{m=0}^{\infty}(2-\delta_{0m})R^m(\tau;\mu,\mu_0)\cos m(\phi-\phi_0), \quad (7)$$

where

$$\delta_{0m} = 1 \quad \text{for } m = 0$$
$$= 0 \quad \text{for } m \neq 0. \quad (8)$$

Thus each $R^m(\tau;\mu,\mu_0)$ satisfies its own equation:

$$\frac{\partial R^m(\tau;\mu,\mu_0)}{\partial\tau} = -\left(\frac{1}{\mu}+\frac{1}{\mu_0}\right)R^m(\tau;\mu,\mu_0) + \frac{\varpi}{4\mu\mu_0}P^m(-\mu,\mu_0)$$
$$+\frac{\varpi}{2\mu_0}\int_0^1 R^m(\tau;\mu,\mu')P^m(\mu',\mu_0)d\mu' + \frac{\varpi}{2\mu}\int_0^1 P^m(-\mu,-\mu')R^m(\tau;\mu',\mu_0)d\mu'$$
$$+\varpi\int_0^1 R^m(\tau;\mu,\mu')\left[\int_0^1 P^m(\mu',-\mu'')R^m(\tau;\mu'',\mu_0)d\mu''\right]d\mu'. \quad (9)$$

This equation can be solved by applying a numerical quadrature technique to the μ-integrations, which yields the set of equations

$$\frac{\partial R^m(\tau;\mu_i,\mu_j)}{\partial\tau} = -\left(\frac{1}{\mu_i}+\frac{1}{\mu_j}\right)R^m(\tau;\mu_i,\mu_j) + \frac{\varpi}{4\mu_i\mu_j}P^m(-\mu_i,\mu_j)$$
$$+\frac{\varpi}{2\mu_j}\sum_{k=1}^{N}R^m(\tau;\mu_i,\mu_k)P^m(\mu_k,\mu_j)w_k + \frac{\varpi}{2\mu_i}\sum_{k=1}^{N}P^m(-\mu_i,-\mu_k)R^m(\tau;\mu_k,\mu_j)w_k$$
$$+\varpi\sum_{k=1}^{N}R^m(\tau;\mu_i,\mu_k)\left[\sum_{l=1}^{N}P^m(\mu_k,-\mu_l)R^m(\tau;\mu_l,\mu_j)w_l\right]w_k. \quad (10)$$

The μ_k and w_k are the divisions and weights for the quadrature. N is the number of quadrature divisions on the

interval (0, 1), and thus (10) represents N^2 equations. However, because of the symmetry relation (Hovenier 1969; Hansen and Travis 1974*a*)

$$R^m(\tau; \mu_i, \mu_j) = R^m(\tau; \mu_j, \mu_i) \tag{11}$$

the number of simultaneous equations that must be solved is $N(N + 1)/2$.

A typical method for solving (10) is to use Gauss quadrature for the μ-integration and a Runge-Kutta method for the τ-integration (Bellman, Kalaba, and Prestrud 1963; Kagiwada, Kalaba, and Ueno 1975). The number of divisions required in the μ-integration is determined by the anisotropy of the phase function and is typically $N \approx$ 5–20. The necessity for using a very large value of N can be avoided by using a phase function renormalization procedure for the finite number of angles and, in the case of a phase function with a sharp diffraction peak, by truncating the diffraction peak and appropriately rescaling ϖ and τ; both techniques are described by Hansen (1971). We tried a few μ-integration methods, but we did not find any that were significantly superior to Gauss quadrature, despite the handicap of having some very small μ_k in that method (cf. discussion below).

The primary difficulty with the invariant imbedding method is the very large number of steps required in the τ-integration. Empirically it is found that to maintain convergence with the Runge-Kutta method the step size must be $\Delta\tau \lesssim 0.1/N$. Thus on the order of 10^3 steps are typically required to reach $\tau = 10$. This compares to $\sim$20 steps for the doubling method. None of the many τ integration methods closely related to the Runge-Kutta method (e.g., Adams-Bashforth, Adams-Moulton) significantly alters this comparison. However, the techniques described in the next two sections reduce the computing time to a value of the same order as that for the doubling method.

III. STIFF EQUATION TECHNIQUE

It is useful to rewrite the invariant imbedding equation (9) in the shorthand notation

$$\frac{\partial R(\tau)}{\partial \tau} = -CR(\tau) + F(\tau)\,, \tag{12}$$

where

$$C \equiv \frac{1}{\mu} + \frac{1}{\mu_0}\,, \tag{13}$$

$$R(\tau) \equiv R^m(\tau; \mu, \mu_0)\,, \tag{14}$$

$$F(\tau) \equiv \varpi\left\{\frac{1}{4\mu\mu_0} P^m(-\mu, \mu_0) + \frac{1}{2\mu_0}\int_0^1 R^m(\tau; \mu, \mu')P^m(\mu', \mu_0)d\mu' + \frac{1}{2\mu}\int_0^1 P^m(-\mu, -\mu')R^m(\tau; \mu', \mu_0)d\mu'\right.$$
$$\left. + \int_0^1 R^m(\tau; \mu, \mu')\left[\int_0^1 P^m(\mu', -\mu'')R^m(\tau; \mu'', \mu_0)d\mu''\right]d\mu'\right\}. \tag{15}$$

The source of difficulty in solving equation (12) is that it is a so-called "stiff" differential equation: the "time constant" C takes on large values, and this requires very small steps in τ if a conventional integration scheme is used. One technique for efficiently solving such a stiff equation is to separate the part of the solution which exponentially damps out with a power proportional to the large time constant, and approximate the source term (i.e., F in [12]) with a polynomial in τ, thus permitting the τ-integration to be performed explicitly (Certaine 1960).

The formal solution of (12) is

$$R(\tau_2) = \exp\,[-C(\tau_2 - \tau_1)]R(\tau_1) + \int_{\tau_1}^{\tau_2} \exp\,[-C(\tau_2 - \tau')]F(\tau')d\tau'\,. \tag{16}$$

Approximating $F(\tau')$ by a polynomial in τ' of degree $\Lambda + 1$,

$$F(\tau') \approx \sum_{\lambda=0}^{\Lambda} \frac{(\tau' - \tau_1)^\lambda}{\lambda!(\tau_2 - \tau_1)^\lambda}\, a_\lambda\,, \tag{17}$$

yields

$$\int_{\tau_1}^{\tau_2} \exp\,[-C(\tau_2 - \tau')]F(\tau')d\tau' \approx \sum_{\lambda=0}^{\Lambda} a_\lambda f_\lambda\,, \tag{18}$$

where

$$f_0 = \{1 - \exp\,[-C(\tau_2 - \tau_1)]\}/C\,, \tag{19}$$

$$f_{\lambda+1} = [1/(\lambda + 1)! - f_\lambda/(\tau_2 - \tau_1)]/C\,. \tag{20}$$

The constants a_λ should be determined from the $\Lambda + 1$ values of $F(\tau)$. We take $\Lambda = 1$ for the first step in τ and $\Lambda = 2$ for subsequent steps. For $\Lambda = 1$,

$$F(\tau_1) = a_0, \quad F(\tau_2) = a_0 + a_1; \tag{21}$$

thus for the first step

$$R(\tau_2) = \exp[-C(\tau_2 - \tau_1)]R(\tau_1) + (f_0 - f_1)F(\tau_1) + f_1F(\tau_2). \tag{22}$$

For subsequent steps we assume that the solution is known at two optical depths, τ_1 and τ_2, and is desired at τ_3, where $\tau_3 - \tau_2$ is not necessarily equal to $\tau_2 - \tau_1$. For these steps

$$\begin{aligned} F(\tau_1) &= a_0 - \frac{h_1}{h_2}a_1 + \left[\frac{h_1}{h_2}\right]^2 \frac{a_2}{2}, \\ F(\tau_2) &= a_0, \\ F(\tau_3) &= a_0 + a_1 + a_2/2, \end{aligned} \tag{23}$$

where $h_1 \equiv \tau_2 - \tau_1$ and $h_2 \equiv \tau_3 - \tau_2$; thus

$$\begin{aligned} R(\tau_3) = \exp[-Ch_2]R(\tau_2) + \frac{h_2^2(-f_1 + 2f_2)}{h_1(h_1 + h_2)}F(\tau_1) + \left[f_0 + \frac{(h_2 - h_1)f_1 - 2h_2f_2}{h_1}\right]F(\tau_2) \\ + \frac{h_1}{(h_2 + h_1)}\left[f_1 + \frac{2h_2f_2}{h_1}\right]F(\tau_3). \end{aligned} \tag{24}$$

An iteration is required to obtain $R(\tau_3)$ because $F(\tau_3)$ involves $R(\tau_3)$. However, in practice this usually turns out to be a one-step iteration. The first step, from τ_1 to τ_2, is made by taking as an initial estimate (cf. [22])

$$R(\tau_2) \approx \exp[-C(\tau_2 - \tau_1)]R(\tau_1) + f_0F(\tau_1). \tag{25}$$

This estimate for $R(\tau_2)$ is then substituted into the right-hand side of (22) with the iteration continued to convergence. The initial estimate of $R(\tau_3)$ for the step from τ_2 to τ_3, as well as the initial estimate of $R(\tau_n)$ for all subsequent steps, is obtained as a linear extrapolation in τ of the solutions at the preceding two steps:

$$R(\tau_n) \approx [R(\tau_{n-1}) - R(\tau_{n-2})]h_{n-1}/h_{n-2} + R(\tau_{n-1}). \tag{26}$$

With $n = 3$, formula (26) provides the first estimate for $R(\tau_3)$ and thus, by means of (24), the second estimate of $R(\tau_3)$. Iteration is continued until

$$\text{Max}\,|1 - R_n^{\text{new}}/R_n^{\text{old}}| \leq \epsilon, \tag{27}$$

where Max signifies the maximum value over all combinations of μ and μ_0, and where ϵ is a small number specified in accordance with the accuracy required, as described in the following section.

An important feature of the technique developed here is that it permits a varying increment in the optical depth integration. This is essential for optimizing the computing speed.

IV. OPTICAL DEPTH LIMIT

For an optically thick atmosphere the computation time can be minimized by restricting the computations to the effective part of the atmosphere. Hansen and Travis (1974*a*) have shown that the depth of the atmosphere contributing to the reflection function decreases rapidly for the higher terms in a Fourier expansion of the reflection function. Thus although an optical depth ~ 100 may contribute to the first (azimuth independent) term in the expansion for conservative or nearly conservative scattering ($\varpi \sim 1$), most of the higher terms arise from the upper skin of the atmosphere, i.e., at optical depths $\tau \lesssim 1$. For a homogeneous atmosphere it is trivial to take advantage of this situation; it is only necessary to stop the computations for each Fourier term after its change with increasing τ becomes sufficiently small. However, since the atmosphere is built from the ground up with the usual invariant imbedding method, for an inhomogeneous atmosphere it is necessary to choose *a priori* the optical depth at which to begin the computations. (An alternative procedure would be to use the two invariant imbedding equations obtained by adding a thin layer to the bottom of the atmosphere, [3.53] and [3.54] of Hansen and Travis 1974*a*, to numerically solve simultaneously for R and T, thus building an atmosphere from the top down. Those two equations each involve both R and T; thus the procedure would necessarily yield both the reflection and transmission, at the expense of additional computing time and programming complexity.)

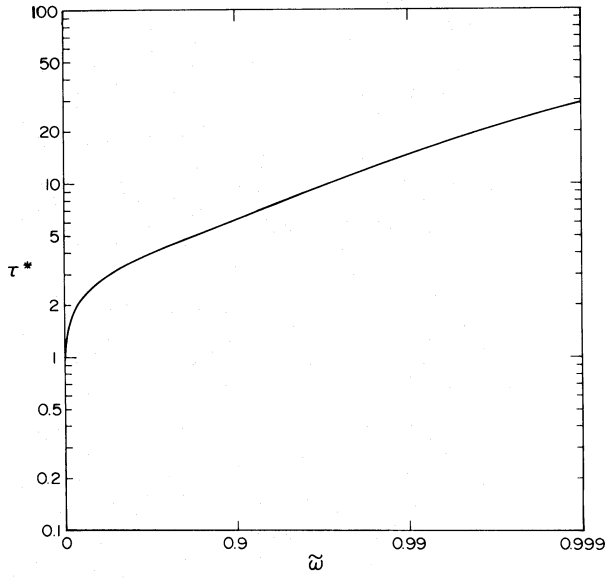

FIG. 3.—Optical thickness τ^* for which $|\partial R/\partial\tau|$ becomes less than 0.001 at all (μ, μ_0) for isotropic scattering in a homogeneous atmosphere. The quantity ϖ is the single scattering albedo. For $\varpi = 1$, not shown in the figure, $\tau^* \approx 45$.

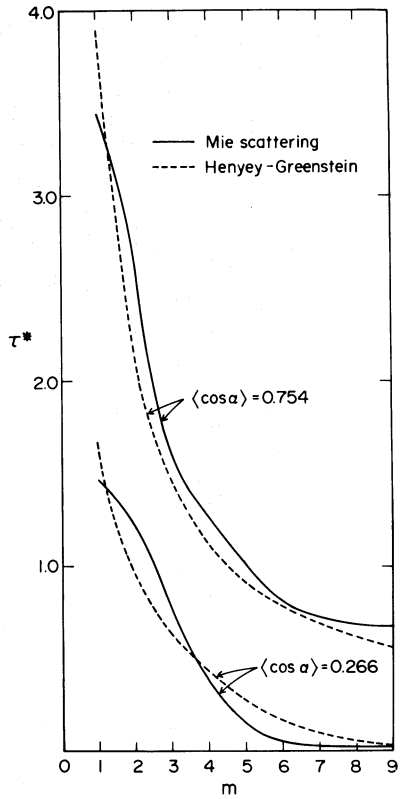

Fig. 4.—Optical thickness τ^* for which $|\partial R/\partial\tau|$ becomes less than 0.001 at all (μ, μ_0) for anisotropic scattering in an inhomogeneous atmosphere. The Mie scattering results are for size parameters $2\pi a/\lambda = 1$ and 10, which lead to anisotropy parameters $\langle\cos\alpha\rangle = 0.266$ and 0.754, respectively. The Henyey-Greenstein results are for the same values of $\langle\cos\alpha\rangle$. The quantity m is the index in the Fourier expansion.

Figure 3 shows the optical thickness τ^* for which $|\partial R/\partial\tau|$ becomes less than 10^{-3} for all (μ, μ_0) for isotropic scattering in a homogeneous atmosphere. There is only one Fourier term for isotropic scattering, so τ^* is a function of only one parameter, ϖ.

For anisotropic scattering the optical thickness required to yield some specified convergence, τ^*, must depend on the phase function as well as on ϖ. We can anticipate from similarity considerations (van de Hulst 1968; van de Hulst and Grossman 1968; Hansen 1969) that the dependence will be primarily on the anisotropy parameter of the phase function, $\langle\cos\alpha\rangle$ (cf. Hansen and Travis 1974*a*), rather than the detailed shape of the phase function. Figure 4 provides some confirmation of this by comparing τ^* (defined quantitatively as above) for Henyey-Greenstein and Mie functions having the same value for $\langle\cos\alpha\rangle$. The Henyey-Greenstein phase functions are given by

$$P(\alpha) = \frac{1 - g^2}{(1 + g^2 - 2g\cos\alpha)^{3/2}} \tag{28}$$

with $g \equiv \langle\cos\alpha\rangle$ and the Mie phase functions are computed for spheres of real refractive index 1.33 and size distribution

$$n(r) = \text{constant}\ r^{(1-3b)/b}e^{-r/ab} \tag{29}$$

with $b = 0.05$ and $2\pi a/\lambda = 1$ and 10, where λ is the wavelength (cf. Hansen and Travis 1974*a*).

It is useful to have analytic representations for the τ^* required to obtain some practical accuracy for R, say a few tenths of 1%. Empirically we find that the formula

$$\tau^* = \frac{3}{m(1 - \langle\cos\alpha\rangle)^{2/3}}\exp(-m/m^*) \quad [m > 0], \tag{30}$$

where

$$m^* = 20\langle\cos\alpha\rangle(1 + 2\langle\cos\alpha\rangle)$$

is adequate for all ϖ for the azimuth-dependent terms. For the azimuth independent term we use

$$\tau^* = \frac{3}{(1 - \varpi + 0.0003)^{1/3}(1 - \langle\cos\alpha\rangle)} \quad [m = 0], \tag{31}$$

where the second term in (31), excluding the factor $(1 - \langle\cos\alpha\rangle)$ is an approximate fit to the curve in Figure 3 for isotropic scattering. For an inhomogeneous atmosphere, equations (30) and (31) can be used by choosing ϖ and $\langle\cos\alpha\rangle$ at an effective optical depth, say at $\tau = 1$.

V. TIMING AND ACCURACY TESTS

To illustrate the speed and accuracy of this new invariant imbedding method we can make comparisons with the doubling program published by Hansen and Travis (1974*b*). This provides a fairly stiff test since the latter program has been optimized for computing speed; its accuracy has also been checked in a number of ways and is known to be capable of yielding results correct to several significant digits.

With both the doubling and invariant imbedding methods we illustrate two cases, case A in which computational parameters have been specified loosely to obtain rapid computations and an accuracy of the order of 1%, and case B with tight computational parameters which should yield an accuracy within a few hundredths of 1%.

Representative timing comparisons are shown in Table 1, and accuracies are indicated by the results in Table 2. The Henyey-Greenstein phase function, (28), with $g = 0.75$ was employed, and the single scattering albedo was $\varpi = 1$. The number of Gauss points was 15 for all the computations. The computational parameters for the doubling method are defined by Hansen and Travis (1974*b*). The doubling method is typically 2 or 3 times faster than the invariant imbedding method for a homogeneous atmosphere. For case A the computational parameters were specified somewhat too loosely for the doubling method, and thus the resulting accuracies are inferior, as indicated by Table 2, and the computing times for the doubling method case A are somewhat smaller than they would be for a case with appropriate accuracy.

For a continuously inhomogeneous atmosphere the invariant imbedding method becomes substantially more efficient than the doubling method. In a computation for a realistic inhomogeneous atmosphere, such as the example in the following section, the upper layers ($\tau \lesssim 1$) strongly influence the reflection function. Thus with the invariant imbedding method it is appropriate in the case of an inhomogeneous atmosphere to reverse the process of increasing the optical thickness of each added layer when the midpoint of the layer is reached, and from there to the top of the atmosphere decrease the size of each step; the total computing time thus increases by almost a factor 2 compared to the homogeneous case. However, with the "doubling and adding" method the atmosphere must be approximated by a large number (say N) of homogeneous layers which are each treated with the doubling method and then added together; the total computing time thus increased by almost a factor N compared to the homogeneous case.

TABLE 1

TIMING COMPARISONS OF THE DOUBLING AND INVARIANT IMBEDDING METHODS

	Fourier Term					
						All m
	0	1	5	10	14	0–14
	$\tau = 1$					
Doubling (A)	0.35	0.22	0.13	0.13	0.13	2.48
Doubling (B)	0.60	0.60	0.55	0.52	0.50	8.10
Invariant imbedding (A)	0.70	0.73	0.55	0.35	0.25	7.02
Invariant imbedding (B)	1.31	1.32	1.10	0.77	0.62	14.52
	$\tau = 64$					
Doubling (A)	0.45	0.32	0.20	0.20	0.20	3.59
Doubling (B)	0.77	0.75	0.66	0.60	0.60	9.86
Invariant imbedding (A)	4.25	1.55	0.55	0.35	0.25	12.00
Invariant imbedding (B)	5.31	2.30	1.10	0.77	0.62	20.36

	Computational Parameters						
	MCAP	NCAP	NCAP2	NTAU	NTAU2	NORDER	MTOT
Doubling (A)	15	3	2	15	10	2	4
Doubling (B)	15	10	10	25	25	2	15

	$\Delta\tau_{\text{initial}}$	$\Delta\tau^{\text{new}}/\Delta\tau^{\text{old}}$	ϵ
Invariant imbedding (A)	0.05	1.050	0.0001
Invariant imbedding (B)	0.01	1.047	0.0001

NOTE.—Times are in seconds on an IBM 360/95, a computer which is approximately a factor 1.5–2 slower than a CDC 7600.

VI. APPLICATION TO VENUS

As an illustration of the fast invariant imbedding method, we perform computations of the equivalent widths of CO_2 absorption lines in solar radiation reflected by Venus for several models of the atmosphere of Venus. This is a problem which has been extensively studied in planetary astronomy, for example, by Chamberlain and Kuiper (1956) and Chamberlain and Smith (1970) for isotropic scattering, by Hunt (1972*a*, *b*) for an inhomogeneous atmosphere with the Henyey-Greenstein phase function, and by Whitehill and Hansen (1973) for a homogeneous atmosphere with Mie scattering phase functions. We make computations for the $R(0)$ line of the 0.782 μm CO_2 band and the $R(0)$ of the 1.049 μm CO_2 band and compare the results with observations of Young (1972).

a) General Computational Details

The atmospheric temperature profile as a function of altitude is taken from Lacis (1976) and is shown in Figure 5. It is based on *Venera-8* data for altitudes $h < 50$ km and *Mariner-10* data for $h > 50$ km.

The gaseous composition is taken as 100% CO_2. The gaseous absorption coefficient k_ν is assumed to have the Lorentz line shape

$$k_\nu = \frac{S(T)\gamma(P, T)}{\pi[(\nu - \nu_0)^2 + \gamma(P, T)^2]} . \tag{32}$$

The half-width,

$$\gamma = \gamma_0 \frac{P}{P_0} \left(\frac{T_0}{T}\right)^{1/2} , \tag{33}$$

is specified by $\gamma_0 = 0.12\ \text{cm}^{-1}$ for the reference temperature and pressure, $T_0 = 251$ K and $P_0 = 1$ bar. The line strengths of the $R(J)$ lines are given by

$$S_J(T) = S_b \frac{J + 1}{Q_{\text{rot}}(T)} \exp\left[-BhcJ(J + 1)/kT\right] , \tag{34}$$

TABLE 2

REFLECTION FUNCTIONS COMPUTED FOR THE FOUR CASES DESCRIBED IN TABLE 1

	$\tau = 1$		$\tau = 64$	
	$\varpi = 0.95$	$\varpi = 1$	$\varpi = 0.95$	$\varpi = 1$
		$R(0.1, 0.1, 0)$		
Doubling (A)	2.363103	2.534175	2.369377	2.555571
Doubling (B)	2.374785	2.547915	2.381061	2.569317
Invariant imbedding (A)	2.374774	2.547900	2.381046	2.569425
Invariant imbedding (B)	2.374775	2.547906	2.381042	2.569408
		$B(0.1, 0.1, 180)$		
Doubling (A)	0.030469	0.035427	0.035398	0.054672
Doubling (B)	0.034373	0.040044	0.039302	0.059289
Invariant imbedding (A)	0.034368	0.040035	0.039301	0.059421
Invariant imbedding (B)	0.034372	0.040043	0.039301	0.059408
		$R(0.5, 0.5, 0)$		
Doubling (A)	0.271383	0.317666	0.410479	0.692980
Doubling (B)	0.272534	0.319049	0.411804	0.694640
Invariant imbedding (A)	0.272268	0.318677	0.411095	0.695595
Invariant imbedding (B)	0.272501	0.319012	0.411014	0.695303
		$R(0.5, 0.5, 180)$		
Doubling (A)	0.054929	0.067668	0.142508	0.372051
Doubling (B)	0.055508	0.068356	0.143178	0.372850
Invariant imbedding (A)	0.055414	0.068216	0.143203	0.374969
Invariant imbedding (B)	0.055508	0.068356	0.143167	0.374735
		$R(1, 1)$		
Doubling (A)	0.033096	0.039095	0.259546	0.995434
Doubling (B)	0.033096	0.039095	0.259546	0.995466
Invariant imbedding (A)	0.033041	0.039017	0.259554	1.003625
Invariant imbedding (B)	0.033095	0.039094	0.259552	1.002880

so that for the $R(0)$ lines

$$S_0(T) = \frac{S_b}{Q_{\rm rot}(T)}, \tag{35}$$

where S_b is the band strength and $Q_{\rm rot}$ the rotational partition function. We use $S_b = 0.16\ {\rm cm}^{-1}$/km-atm for the 0.782 μm band and $S_b = 6.63\ {\rm cm}^{-1}$/km-atm for the 1.049 μm band (Young 1972), and $Q_{\rm rot} = 223T/T_0$ (Gray and Young 1969).

The cloud particles are assumed to have the properties deduced by Hansen and Hovenier (1974) from the polarization of reflected sunlight. The particle size distribution is given by (29) where a, the effective radius, is 1.05 μm and b, the effective variance, is 0.07. Phase functions $P_c(\alpha)$ computed for $n_r = 1.433$ and $n_i = 1.7 \times 10^{-5}$ at $\lambda = 0.782$ μm, and $n_r = 1.430$ and $n_i = 3.3 \times 10^{-5}$ at $\lambda = 1.049$ μm, are shown in Figure 6. The wavelength dependence of the cloud particle extinction is taken into account, the spectral variation being the same as illustrated in Figure 2 of Lacis (1975).

The Rayleigh scattering optical thickness is $\tau_0 = 17.4$ at wavelength $\lambda = 0.55$ μm (cf. Hansen and Travis 1974*a*). This optical thickness varies with wavelength as $\lambda^{-4}(1 + 0.013\lambda^{-2})$ which includes the spectral dependence of the CO_2 refractive index. The Rayleigh optical thickness above any pressure level P is given by

$$\tau_R = \tau_0(P/P_0), \tag{36}$$

where the surface pressure $P_0 = 93$ atmospheres.

The total optical thickness is

$$\tau = \tau_{\rm cl} + \tau_R + \tau_v, \tag{37}$$

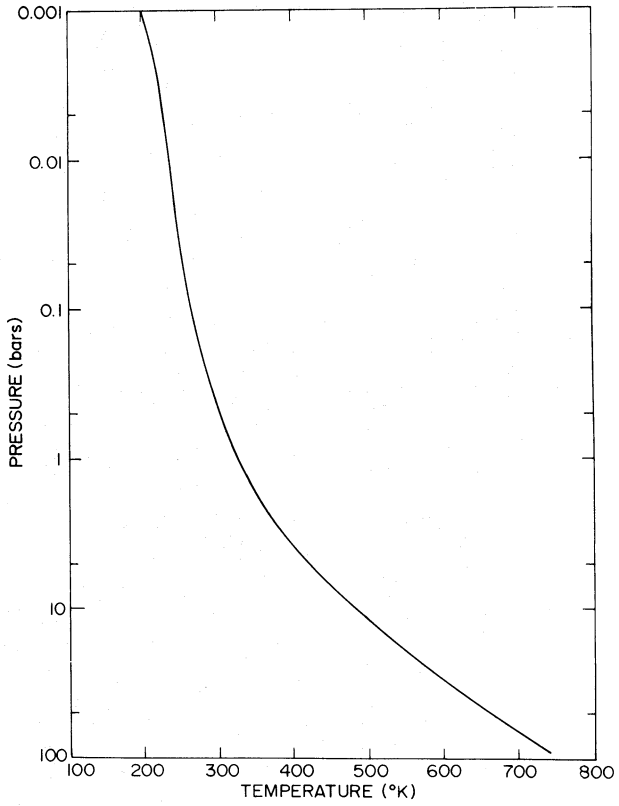

FIG. 5.—Atmospheric temperature profile used in the computations

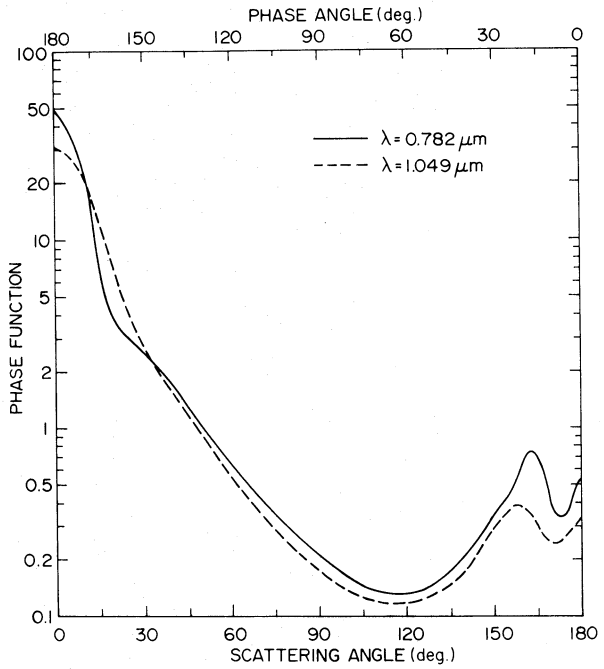

FIG. 6.—Phase functions used in the multiple scattering computations for Figs. 7–11. The refractive indices and the asymmetry parameters are $n_r = 1.433$ and $\langle \cos \alpha \rangle = 0.675$ for $\lambda = 0.782$ μm and $n_r = 1.430$ and $\langle \cos \alpha \rangle = 0.728$ for $\lambda = 1.049$ μm.

where the three contributions arise from the cloud particles, Rayleigh scattering, and gaseous absorption. The single scattering albedo is

$$\varpi = \frac{k_{\mathrm{sca,cl}} + k_R}{k_{\mathrm{sca,cl}} + k_{\mathrm{abs,cl}} + k_R + k_\nu} = \frac{\varpi_{\mathrm{con}}}{1 + k_\nu/(k_{\mathrm{cl}} + k_R)}, \tag{38}$$

where ϖ_{con} is the single scattering albedo in the continuum (where $k_\nu = 0$). The phase function is

$$P(\alpha) = \frac{1}{1+f} P_c(\alpha) + \frac{f}{1+f} P_R(\alpha), \tag{39}$$

where f is the ratio of the Rayleigh and cloud scattering coefficients,

$$f = k_{\mathrm{sca},R}/k_{\mathrm{sca,cl}}.$$

The intensity of the reflected radiation was integrated over the illuminated part of the planetary intensity equator, to simulate the slit orientation for most of the observations. The equivalent width was computed as

$$W = \int_0^\infty \frac{I_c - I_\nu}{I_c}\, d\nu, \tag{40}$$

where I_c and I_ν are the intensity in the continuum and at the frequency ν within the line. Since the true continuum is often difficult to determine precisely, we also made computations to levels defined as a fraction (for example, 95% or 99%) of the theoretical continuum.

b) Specific Atmospheric Models

Computations were made for four models of the atmosphere: a reflecting layer model, a homogeneous atmosphere model, a model constructed by Lacis (1975) from pre-*Venera-9* and -*10* data and a model based on *Venera-9* cloud particle nephelometer measurements. The cloud particle number densities as a function of altitude are illustrated in Figure 7.

The reflecting layer model has an opaque Lambert (isotropically reflecting) surface of reflectivity R_c at the cloud-top pressure level P_c, which are thus the two parameters in this model. For the computations illustrated we put the cloud-top at $P_c = 300$ mb, as required to yield the observed order of magnitude for CO_2 equivalent widths, and we chose R_c to yield the observed albedo of Venus in the continuum near each absorption band (~94% at $\lambda = 0.782\ \mu$m and ~88% at $\lambda = 1.049\ \mu$m; cf., Travis 1975).

The homogeneous atmosphere model employs a homogeneous mixture of CO_2 molecules and cloud particles. The model has three parameters: the ratio of Rayleigh and cloud opacity at $\lambda = 0.365\ \mu$m (f), the ground

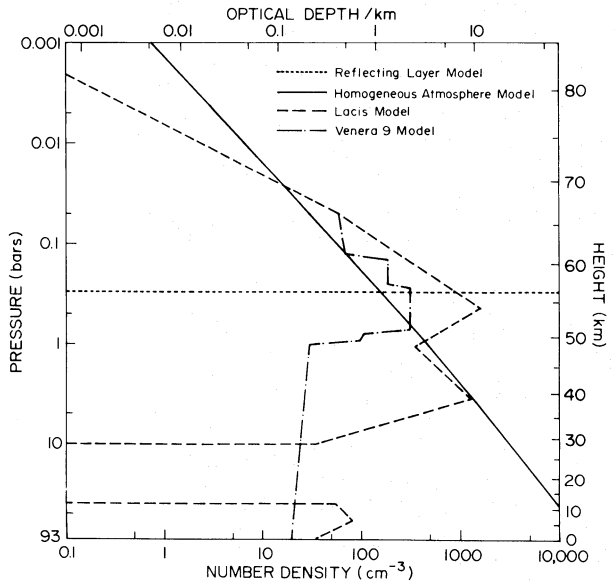

FIG. 7.—Vertical distributions of cloud particles in the models employed for multiple scattering computations. The number densities are based on the assumption of 1.05 μm particles throughout the atmosphere. The optical depth per km (extinction coefficient per unit volume), shown on the upper scale for $\lambda = 0.782\ \mu$m is the more significant physical quantity.

TABLE 3

Venera-9 DATA FOR THE CLOUD OPTICAL THICKNESS AT $\lambda \approx 0.9$ μm

Height (km)	Optical Thickness
61–57	6
57–51	15
51–49	2
49–18	6

reflectivity (R_g), and the cloud-particle single scattering albedo (ϖ^{cl}). We take $f = 0.045$ as given by polarization analyses (Hansen and Hovenier 1974), which corresponds to a specific abundance of 0.24 km-atm (6.7×10^{23} molecules cm^{-2}) at $\lambda = 0.782$ μm and 0.19 km-atm (5.1×10^{23} molecules cm^{-2}) at $\lambda = 1.049$ μm. Because of the resulting optically thick atmosphere, the CO_2 equivalent widths are not sensitive to R_g; we take $R_g = 0.1$, in the range (0.02–0.2) determined by *Venera-9* and *Venera-10* (Keldysh 1976). The single scattering albedo is taken as $\varpi^{cl} = 0.99977$ at $\lambda = 0.782$ μm and $\varpi^{cl} = 0.99921$ at $\lambda = 1.049$ μm to yield the observed spherical albedos.

The inhomogeneous cloud model adopted from Lacis (1975) is based on *Mariner-10*, *Venera-8*, and ground-based observations. The vertical distribution of cloud particles is compared in Figure 7 to the homogeneous atmosphere model. Within each of the several layers in Lacis's model the ratio of the gas scale height to the cloud particle scale height, $m \equiv H_{gas}/H_{cl}$, is constant. Since the cloud distribution is specified, the only parameters in this model are the ground albedo and single scattering albedo of the cloud particles. This model atmosphere is also so optically thick that the reflectivity is not sensitive to the ground albedo. For the single scattering albedo we use $\varpi^{cl} = 0.99973$ at $\lambda = 0.782$ μm and $\varpi^{cl} = 0.99918$ at $\lambda = 1.049$ μm.

The final model considered is based on *Venera-9* nephelometer results (Marov *et al.* 1976) for altitudes below 61 km combined with Lacis's model at higher altitudes. The graphical data of Marov *et al.* were smoothed, yielding the distribution illustrated in Figure 7. The optical thickness within different height intervals below 61 km is specified in Table 3. The cloud-particle scale height between 61 and 67 km is chosen to yield convergence to Lacis's model at 67 km (50 mb), above which level the cloud optical thickness is rather accurately known from ground-based polarimetry. The total cloud optical thickness is 32 at $\lambda = 0.782$ μm and 40 at $\lambda = 1.049$ μm. Because of this moderate optical thickness we take $\varpi^{cl} = 1$ and $R_g = 0.2$ at $\lambda = 0.792$ μm, which yield a spherical albedo ($\sim$92%) close to that observed. At $\lambda = 1.049$ μm we use $R_g = 0.1$ and $\varpi = 0.9996$ which yield $A \approx 88\%$.

c) *Numerical Results*

We first present some results with the homogeneous atmosphere model, which provide conclusions of general applicability.

Figure 8 illustrates the equivalent width of the $R(0)$ line in the 0.782 μm band for two versions of the "homogeneous" model: one, as described above, in which the band strength varies with temperature and the line half-width varies with temperature and pressure, and a second version in which $S_0 = 6.8 \times 10^{-2}$ cm^{-1}/km-atm and $\gamma = 0.0145$ cm^{-1} (appropriate for $P = 125$ mb, $T = 267$ K). Figure 9 illustrates the absorption line profiles for the same cases at two planetary phase angles ($\alpha = 60°$ and 160°).

These results indicate that it is generally not adequate to analyze planetary spectra with a model employing an average temperature and pressure, although that procedure has often been used. Even though it is possible to find an appropriate constant temperature and pressure to match the equivalent width of the line in a given situation, different values would certainly be required for lines of different strengths. A reliable interpretation of planetary absorption lines must properly account for pressure and temperature variations with altitude.

Figure 10, also for the homogeneous atmosphere model, illustrates another problem in interpreting actual observations. The equivalent width of the line is seen to depend strongly on the accuracy with which the continuum can be defined. This is primarily a result of the fact that a large fraction of the equivalent width is contained in the line wings. Thus the problem could be partly overcome by defining equivalent widths in both measurements and computations for some finite interval $\Delta\nu$ about the line center; although this does not help locate the continuum, the percentage uncertainty in this equivalent width would be reduced.

It is apparent from the above results that quantitative analysis of atmospheric structure from absorption line measurements should be based on the line shape and band shape, not just on equivalent widths. It is nearly impossible to make unique interpretations from only equivalent widths. Most of the potential information on atmospheric structure is discarded in the integration over frequency. Of course, it is a major observational problem to obtain spectral resolution sufficiently high that the instrumental broadening does not dominate the line shape and central depth of the lines.

Figures 11 and 12 show the equivalent widths of the $R(0)$ lines in the 0.782 μm and 1.049 μm CO_2 bands for the four models described in the preceding subsection. The continuum levels for these two lines are respectively set at 99% and 95% of the theoretical continuum, representing our estimate of the region included in the measured

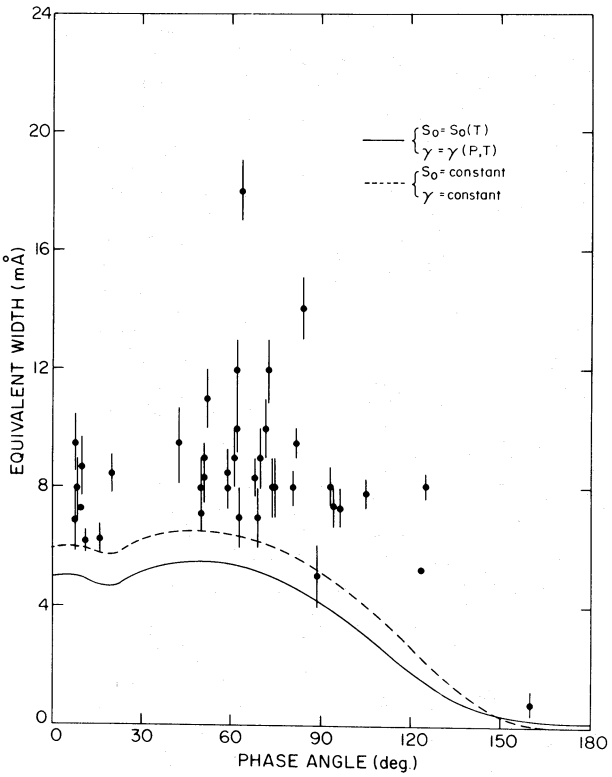

FIG. 8.—Equivalent width of the $R(0)$ line of the 0.782 μm CO_2 band for two versions of the "homogeneous" model. In both cases the cloud particles are uniformly mixed with the gas. In one case (*solid line*) the absorption coefficient is independent of depth in the atmosphere, while in the other case a realistic variation of temperature and pressure with depth (Fig. 5) is employed. The observed equivalent widths are taken from Fig. 4 of Young (1972).

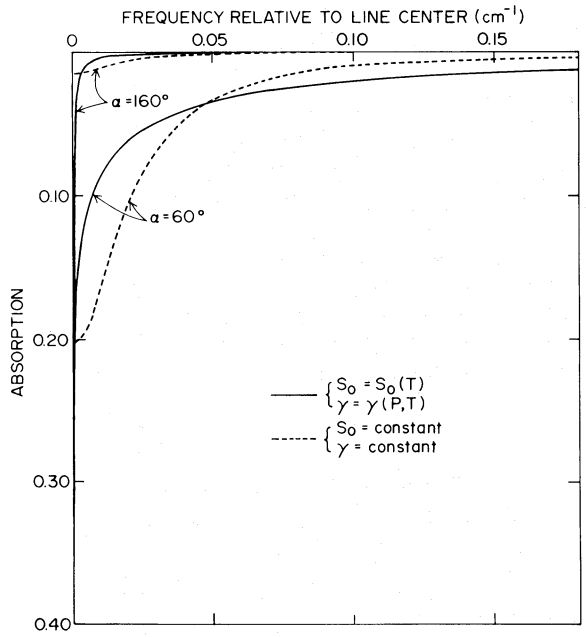

FIG. 9.—Absorption line profiles for the same cases as in Fig. 7, at phase angles 60° and 160°

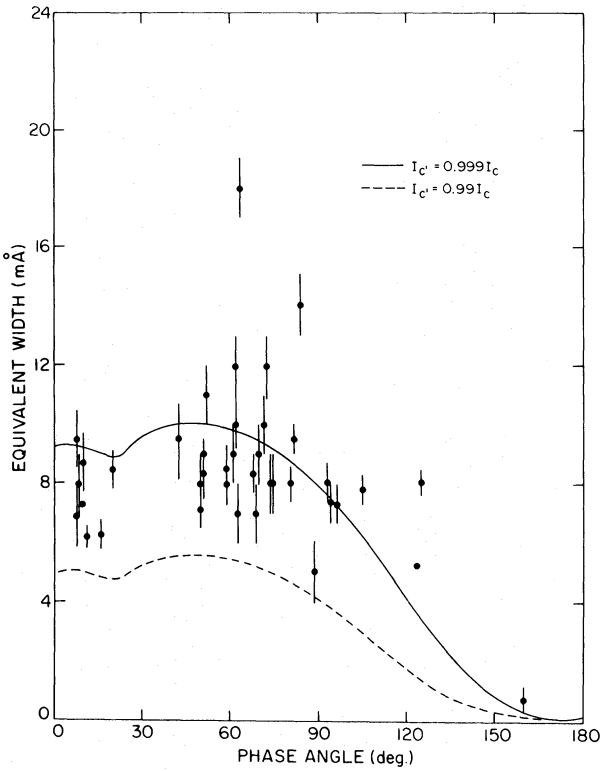

FIG. 10.—Equivalent width of the $R(0)$ line of the 0.782 μm CO_2 band for homogeneous model with two different values for the level of the continuum. The observed equivalent widths are taken from Fig. 4 of Young (1972).

equivalent widths; because of the large uncertainty in this procedure it is best to compare the shape of the equivalent width as a function of phase angle, rather than the absolute value.

Obviously the reflecting layer model cannot fit the observed equivalent widths, a conclusion reached by Chamberlain and Kuiper (1956) on the basis of far fewer data. The homogeneous model, including the effects of pressure and temperature variations on S_0 and γ, is much closer to the observations, but tends to have a too rapid decrease in equivalent width with increasing phase angle. The two inhomogeneous models are better in this regard, primarily because in these models the cloud-particle number density falls off more rapidly (i.e., has a smaller scale height) above 67 km than does the gaseous number density.

In terms of the absolute values of the equivalent widths the model based on *Venera-9* data (below 61 km) provides the closest fit to the observed data. It has a larger equivalent width than the homogeneous model at $\lambda = 0.782$ μm and a smaller equivalent width at $\lambda = 1.049$ μm, results that can be understood on the basis of the effective depths of penetration in the two bands. In the weaker band at $\lambda = 0.782$ μm much of the equivalent width is due to gas at altitudes below 50 km, where the small cloud-particle number density in the model based on *Venera-9* data permits significant penetration. The stronger band at 1.049 μm is basically formed at altitudes above 50 km, where the average number density is smaller for the homogeneous model.

The cloud-particle number densities reported for *Venera-10* (Marov *et al.* 1976) are about twice as large as for *Venera-9*. The resulting equivalent widths (not illustrated here) are closer to those for the model based strictly on the number densities of Lacis (1975).

d) Conclusions

We have found that with the fast invariant imbedding method it is practical to make computations for an atmosphere of arbitrary vertical inhomogeneity, including great optical depths.

It is apparent that quantitative interpretation of absorption line observations of planetary atmospheres should be based on inhomogeneous models of the atmospheres, including the temperature and pressure variations with altitude as well as the variation of scattering properties. Observations of high spectral resolution, in combination with realistic inhomogeneous models, have great potential for providing information on vertical atmospheric structure.

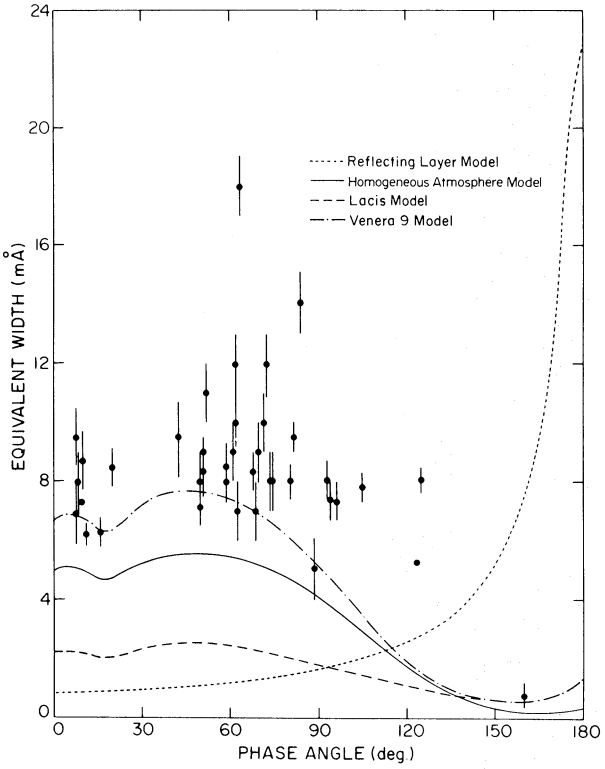

FIG. 11

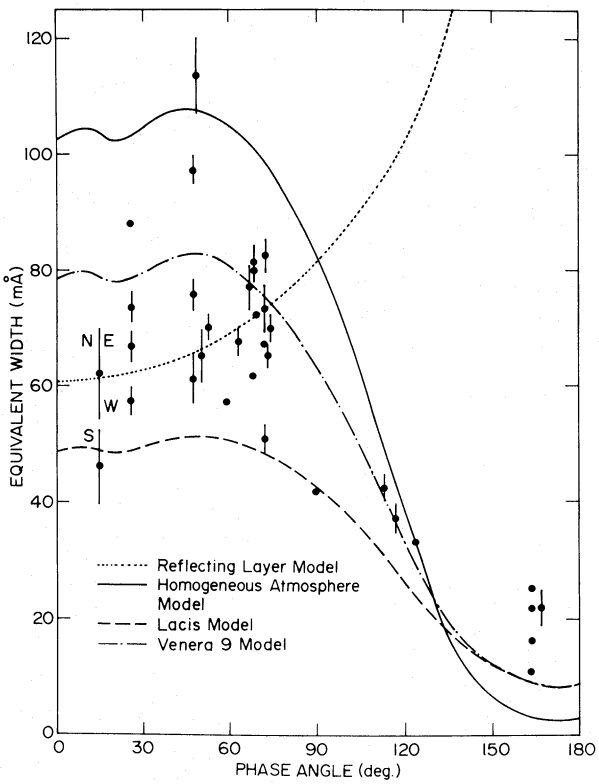

FIG. 12

FIG. 11.—Equivalent width of the $R(0)$ line in the 0.782 μm band, integrated over the illuminated part of the intensity equator. The observed equivalent widths are taken from Fig. 4 of Young (1972).

FIG. 12.—Equivalent width of the $R(0)$ line in the 1.049 μm band, integrated over the illuminated part of the intensity equator. The observed equivalent widths are taken from Fig. 8 of Young (1972).

An inhomogeneous model for Venus, based on *Venera-9* data below 61 km altitude and on the model of Lacis (1975) at higher altitudes, provides a good fit to observed equivalent widths of the $R(0)$ CO_2 lines at 0.782 and 1.049 μm. There are serious limitations in using only these observed equivalent widths for specifying the atmospheric structure, however, and we do not believe that much weight should be placed on this particular result. It should be possible to define the cloud structure with greater confidence on the basis of a more complete analysis of ground-based spectroscopic observations and measurements by several instruments on *Venera-9* and *Venera-10*.

We would like to thank Drs. A. A. Lacis, L. D. Travis, S. Ueno and H. Kagiwada for helpful discussions or comments.

REFERENCES

Ambartsumian, V. A. 1942, *Astr. Zh.*, **19**, 30.
———. 1958, *Theoretical Astrophysics* (New York: Pergamon Press).
Bellman, R. E., Kalaba, R. E., and Prestrud, M. C. 1963, *Invariant Imbedding and Radiative Transfer in Slabs of Finite Thickness* (New York: American Elsevier).
Certaine, J. 1960, in *Mathematical Methods for Digital Computers*, Vol. **1**, ed. A. Ralston and H. S. Wilf (New York: Wiley), p. 128.
Chamberlain, J. W., and Kuiper, G. P. 1956, *Ap. J.*, **139**, 399.
Chamberlain, J. W., and Smith, G. R. 1970, *Ap. J.*, **160**, 755.
Chandrasekhar, S. 1960, *Radiative Transfer* (New York: Dover).
Gray, L. D., and Young, A. T. 1969, *J. Quant. Spectrosc. Rad. Transf.*, **9**, 569.
Hansen, J. E. 1969, *Ap. J.*, **158**, 337.
———. 1971, *J. Atmos. Sci.*, **28**, 1400.
Hansen, J. E., and Hovenier, J. W. 1974, *J. Atmos. Sci.*, **31**, 1137.
Hansen, J. E., and Travis, L. D. 1974*a*, *Space Sci. Rev.*, **16**, 527.
———. 1974*b*, *NASA Institute for Space Studies Report* (New York: NASA).
Hovenier, J. W. 1969, *J. Atmos. Sci.*, **26**, 488.
Hunt, G. E. 1972*a*, *J. Quant. Spectrosc. Rad. Transf.*, **12**, 387.
———. 1972*b*, *J. Quant. Spectrosc. Rad. Transf.*, **12**, 405.
Kagiwada, H. H., Kalaba, R., and Ueno, S. 1975, *Multiple Scattering Processes: Inverse and Direct* (Reading, Mass.: Addison-Wesley).
Keldysh, M. V. 1976, paper presented at the 19th COSPAR Meeting, Philadelphia, Pa.
Lacis, A. A. 1975, *J. Atmos. Sci.*, **32**, 1107.
———. 1976, private communication.

Marov, M. Ya., Levedev, V. N., Lystsev, V. E., Kuznetsov, I. S., and Popandopulo, G. K. 1976, paper presented at the 19th COSPAR Meeting, Philadelphia, Pa.
Travis, L. D. 1975, *J. Atmos. Sci.*, **32**, 1190.
van de Hulst, H. C. 1968, *Bull. Astr. Institute Netherlands*, **20**, 77.
van de Hulst, H. C., and Grossman, K. 1968, in *The Atmospheres of Venus and Mars*, ed. J. C. Brandt and M. B. McElroy (New York: Gordon & Breach), p. 35.
Whitehill, L. P., and Hansen, J. E. 1973, *Icarus*, **20**, 146.
Young, L. D. G. 1972, *Icarus*, **17**, 632.

JAMES E. HANSEN and KIYOSHI KAWABATA: NASA Institute for Space Studies, Goddard Space Flight Center, 2880 Broadway, New York, NY 10025

MAKIKO SATO: NASA Institute for Space Studies, Goddard Space Flight Center, 2880 Broadway, New York, NY 10025; and Department of Physics, Belfer Graduate School of Science, Yeshiva University, 2495 Amsterdam Avenue, New York, NY 10033